Simulation of a Flow in a Return Channel with a Deswirl Cascade Using Advanced Turbulence Modelling

Patrik Rautaheimo and Timo Siikonen[1]

Abstract. A study of different low-Reynolds number turbulence models used for a highly three dimensional return channel with a deswirl cascade is described. A comparison is made between Chien's $k-\epsilon$ model, Chien's model with a rotational correction, an explicit algebraic Reynolds-stress model by Gatski *et al.*, and a full Reynolds-stress closure by Speziale *et al.* Anisotropic models give better results than isotropic ones. However, in some regions none of the models simulate the flow field correctly.

1 Introduction

In this paper the calculation of a highly three dimensional flow in a return channel with a deswirl cascade is described. Experiments are provided by Concepts ETI, INC. [6]. Both isotropic and anisotropic turbulence models are applied. The problem with linear two-equation models, including Chien's model [2], is that they do not take account of the effect of the streamline curvature and they assume a Reynolds-stress tensor to be aligned with a strain-rate tensor. Models with these limitations are not able to simulate some of the turbulence-driven phenomena, e.g. a secondary flow in a square duct. Anisotropic alternatives such as the Reynolds-stress models have the potential to simulate also that kind of phenomenon.

The geometry of the present test case is given in Fig. 1. The geometry is typically used to join the exit from the first stage of a centrifugal machine to the inlet of the second stage. The flow field is affected by a strong streamline curvature, separations take place and three-dimensional vortices exist. Hence, this case is a highly demanding test for turbulence modelling. Because of the high anisotropy of the flow, it is expected that Reynolds-stress models perform better than a traditional two-equation model.

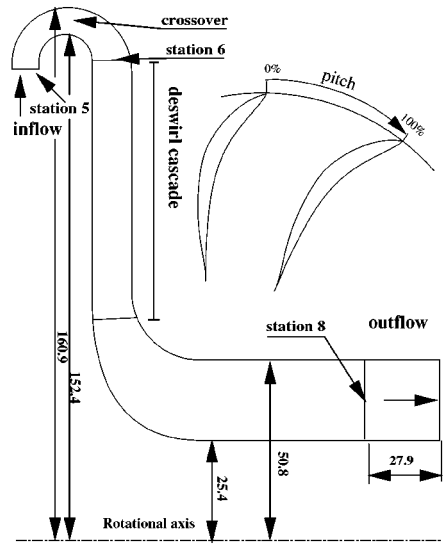

Figure 1. Geometry of the return channel.

2 Basic Features of the Flow Solver

The flow solver utilizes a structured multiblock grid. In each block an implicit LU-factored solution with a multigrid acceleration of convergence is performed. The boundary conditions between the blocks are treated explicitly and only on the highest grid level. In this study the solution method is based on Roe's scheme [11]. The

[1] Laboratory of Applied Thermodynamics, Helsinki University of Technology, P.O.Box 4400, FIN-02015 HUT, Finland

ECCOMAS 98.
Published in 1998 by John Wiley & Sons, Ltd.

Table 1. Functions and constants.

Model	D	c_μ	$c_{\epsilon 1}$	$c_{\epsilon 2}$	σ_k	σ_ϵ
CH	$2\nu k/y_n^2$	0.09	1.44	1.92	1.0	1.3
GS	0	0.088	1.39	1.83	1.0	1.3

f_μ	f_2	E
$1-e^{-0.0115y^+}$	$1-0.22e^{-Re_T^2/36}$	$-2\mu(\tilde{\epsilon}/y_n^2)e^{-0.5y^+}$
1	$1-e^{-Re_y/12.5}$	0

flux calculation utilizes a MUSCL-type differencing with a second-order upwinding in streamwise direction and third-order upwind biased discretization in other directions. Turbulence is modelled either by a two-equation model or by a Reynolds-stress model. The solution methods are described in more detail in Refs. [10, 13, 14].

3 Turbulence Models

Four different low-Reynolds number turbulence models are tested:

- $k-\epsilon$ model of Chien [2] (CH)
- $k-\epsilon$ with a rotational correction [9] (CHR)
- explicit ARSM of Gatski *et al.* [4] (GS)
- RSM of Speziale *et al.* [15] (SSG)

The first one is a classical low-Reynolds number $k-\epsilon$ model, the second is the same model with a rotational correction, the third is an explicit algebraic Reynolds-stress model, and the fourth is a full Reynolds-stress closure.

3.1 $k-\epsilon$ Models

Models based on the solution of k- and ϵ-equations can be written in general form as

$$\mu_T = c_\mu f_\mu \bar{\rho}\frac{k^2}{\tilde{\epsilon}} \quad (1)$$

$$\epsilon = \tilde{\epsilon} + D \quad (2)$$

$$\bar{\rho}\frac{Dk}{Dt} = \frac{\partial}{\partial x_i}\left[(\mu+\mu_T/\sigma_k)\frac{\partial k}{\partial x_i}\right] + P - \bar{\rho}\epsilon \quad (3)$$

$$\bar{\rho}\frac{D\tilde{\epsilon}}{Dt} = \frac{\partial}{\partial x_i}\left[(\mu+\mu_T/\sigma_\epsilon)\frac{\partial \tilde{\epsilon}}{\partial x_i}\right] + c_{\epsilon 1}\frac{\tilde{\epsilon}}{k}P - c_{\epsilon 2} f_2 \frac{\bar{\rho}\tilde{\epsilon}^2}{k} + E \quad (4)$$

Table 1 summarizes functions and constants for the different two-equation turbulence models applied in this study. The production of turbulent kinetic energy P is written without additional modelling

$$P = \bar{\rho}\widetilde{u_i'' u_j''}\frac{\partial \tilde{u}_i}{\partial x_j} \quad (5)$$

where Reynolds stresses $\bar{\rho}\widetilde{u_i'' u_j''}$ are modelled in the CH and CHR model by using the Boussinesq approximation

$$\bar{\rho}\widetilde{u_i'' u_j''} = -2\mu_T S_{ij} + \frac{2}{3}\delta_{ij}\bar{\rho}k \quad (6)$$

Above S_{ij} is the mean strain rate tensor

$$S_{ij} = \frac{1}{2}\left(\frac{\partial \tilde{u}_i}{\partial x_j} + \frac{\partial \tilde{u}_j}{\partial x_i}\right) \quad (7)$$

In the GS model the Reynolds stresses are explicit function of the mean strain rate and the vorticity tensor as

$$\bar{\rho}\widetilde{u_i'' u_j''} = \frac{2}{3}\bar{\rho}k\delta_{ij} - \frac{6(1+\eta^2)\alpha_1}{3+\eta^2+6\xi^2\eta^2+6\xi^2}\bar{\rho}\frac{k^2}{\epsilon}\left[(S_{ij}-\frac{1}{3}S_{kk}\delta_{ij}) + \alpha_4\frac{k}{\epsilon}(S_{ik}W_{kj}+S_{jk}W_{ki}) - \alpha_5\frac{k}{\epsilon}(S_{ik}S_{kj}-\frac{1}{3}S_{kl}S_{kl}\delta_{ij})\right] \quad (8)$$

where the vorticity rate tensor is

$$W_{ij} = \frac{1}{2}\left(\frac{\partial \tilde{u}_i}{\partial x_j} - \frac{\partial \tilde{u}_j}{\partial x_i}\right) \quad (9)$$

In Eq. (8) η and ξ are strain rate invariants defined by

$$\eta = \frac{1}{2}\frac{\alpha_3}{\alpha_1}(S_{ij}S_{ij})^{\frac{1}{2}}\frac{k}{\epsilon} \quad \xi = \frac{1}{2}\frac{\alpha_2}{\alpha_1}(W_{ij}W_{ij})^{\frac{1}{2}}\frac{k}{\epsilon} \quad (10)$$

Above α_1, α_2, α_3, α_4 and α_5 are the constants that assume the values from [1]

$$\alpha_1 = (\tfrac{4}{3}-C_2)g/2 \quad \alpha_2 = (2-C_3)^2 g^2/4$$
$$\alpha_3 = (2-C_4)^2 g^2/4 \quad \alpha_4 = (2-C_4)g/2$$
$$\alpha_5 = (2-C_3)g \quad g = 1/(C_1+C_5-1) \quad (11)$$

where the constants of the pressure-strain model of Speziale et al. [15] are used

$$C_1 = 3.4 \quad C_2 = 0.36 \quad C_3 = 1.25$$
$$C_4 = 0.4 \quad C_5 = 1.88 \quad (12)$$

Chien's $k-\epsilon$ model is tested also with rotation correction [9] (CHR). In the correction used the dissipation equation is modified so that the function f_2 is replaced by

$$f_2 = (1-C_c)\left(1-0.22e^{-Re_T^2/36}\right) \quad (13)$$

where the term C_c has been added to account for Coriolis effects [5]. That term equals to $-0.2\,Ri$. The Richardson number Ri is calculated from

$$Ri = -\omega\,(s-\omega) \tag{14}$$

where the ω and s are nondimensional vorticity and strain rates [7]. The factor -0.2 is an empirically chosen constant.

3.2 Reynolds-Stress Model

The Reynolds-stress model (RSM) can be written in the following form

$$\frac{\partial \bar{\rho}\widetilde{u_i'' u_j''}}{\partial t} + \frac{\partial(\bar{\rho}\tilde{u}_k \widetilde{u_i'' u_j''})}{\partial x_k} = P_{ij} + \Phi_{ij} + D_{ij} - \epsilon_{ij} \tag{15}$$

where P_{ij}, Φ_{ij}, D_{ij} and $\epsilon_{ij}$are the production term, the pressure-strain term, the diffusion term and the dissipation term, respectively.

The production term is exact, whereas the turbulent diffusion, the pressure strain and the dissipation rate must be modelled. In this work the high-Reynolds number modelling is developed by Speziale, Sarkar and Gatski (SSG) [15]. The low-Reynolds number modelling is based on Shima's work [12]. The connection of the low and high Reynolds number regions is done by using a wall damping function. The dissipation transport equation is based on Chien's $k-\epsilon$ model [2].

In the low-Reynolds number model, the pressure-strain and the dissipation rate terms can be connected as

$$\overline{p'\left(\frac{\partial u_i''}{\partial x_j} + \frac{\partial u_j''}{\partial x_i}\right)} - 2\mu\overline{\frac{\partial u_i''}{\partial x_k}\frac{\partial u_j''}{\partial x_k}} = \Phi_{ij} - \epsilon_{ij} = \phi_{ij,1} + \phi_{ij,2} + \phi_{ij,w} - \frac{2}{3}\delta_{ij}\bar{\rho}\epsilon \tag{16}$$

where $\phi_{ij,1}$ represents the fluctuation part of Φ_{ij} and the anisotropic part of ϵ_{ij}, $\phi_{ij,2}$ the mean-strain part of Φ_{ij}, and $\phi_{ij,w}$ takes account of the wall proximity effects. These terms can be written in the following way [12, 15]

$$\phi_{ij,1} = -\left[\bar{C}_1 - (\bar{C}_1 - 2)f_{w,1}\right]\epsilon\, b_{ij} + C_2\,(1-f_{w,1})\,\epsilon\,(b_{ik}\,b_{kj} - \frac{1}{3}\Pi\delta_{ij}) \tag{17}$$

$$\phi_{ij,2} = (C_3 - C_3^*\Pi^{1/2})\bar{\rho}\,k\,S_{ij} + C_4\,\bar{\rho}\,k(b_{ik}\,S_{jk} + b_{jk}\,S_{ik} - \frac{2}{3}b_{kl}\,S_{kl}\delta_{ij}) + C_5\,\bar{\rho}k(b_{ik}\,W_{jk} + b_{jk}\,W_{ik}) \tag{18}$$

$$\phi_{ij,w} = [\alpha\left(P_{ij} - \frac{2}{3}\delta_{ij}P\right) + \gamma\bar{\rho}kS_{ij} + \beta\left(D_{ij} - \frac{2}{3}\delta_{ij}P\right)]f_{w,1} \tag{19}$$

where P_{ij}, D_{ij} and P are

$$P_{ij} = -\left[\bar{\rho}\widetilde{u_i'' u_k''}\frac{\partial \tilde{u}_j}{\partial x_k} + \bar{\rho}\widetilde{u_j'' u_k''}\frac{\partial \tilde{u}_i}{\partial x_k}\right] \tag{20}$$

$$D_{ij} = -\left[\bar{\rho}\widetilde{u_i'' u_k''}\frac{\partial \tilde{u}_k}{\partial x_j} + \bar{\rho}\widetilde{u_j'' u_k''}\frac{\partial \tilde{u}_k}{\partial x_i}\right] \tag{21}$$

$$P = -\bar{\rho}\widetilde{u_k'' u_l''}\frac{\partial \tilde{u}_k}{\partial x_l} \tag{22}$$

$$f_{w,1} = \exp\left[-\left(0.011\frac{\rho\sqrt{k}y_n}{\mu}\right)^4\right] \tag{23}$$

and

$$b_{ij} = \frac{\widetilde{u_i'' u_j''}}{2\,k} - \frac{1}{3}\delta_{ij} \quad \Pi = b_{kl}b_{kl} \tag{24}$$

$$\bar{C}_1 = C_1 + C_1^* P/\epsilon$$

Eqs. (17) -(19) are written in a general form. Different models can be written by changing the constants. The idea is that the constants of Launder *et al.* [8] (LRR) with Shima's low-Reynolds number part are used close to the wall and far away from the wall the SSG model constants are used. For example, C_1 is not a constant but it is changing as

$$C_1 = f_{w,2}C_{1,LRR} + (1-f_{w,2})C_{1,SSG} \tag{25}$$

The same treatment is done also for C_1^*, C_2, C_3, C_3^*, C_4 and C_5 . The constants for different models are

Model	C_1	C_1^*	C_2	C_3	C_3^*	C_4	C_5
LRR	3.0	0.0	0.0	0.8	0.0	1.75	1.31
SSG	3.4	1.80	4.2	0.8	1.30	1.25	0.40

The wall correction values, α, β and γ, and wall damping function $f_{w,2}$ were assigned after test calculations with a simple channel test case as

$$\alpha = 0.45 \quad \beta = 0 \quad \gamma = 0.04 \tag{26}$$

$$f_{w,2} = \exp\left[-\left(0.015\frac{\rho\sqrt{k}y_n}{\mu}\right)^4\right] \tag{27}$$

In this work a simple scalar diffusion [3] is applied

$$D_{ij} = \frac{\partial}{\partial x_k}\left[(\mu + \mu_T/\sigma_{ij,T})\frac{\partial \widetilde{u_i'' u_j''}}{\partial x_k}\right] \tag{28}$$

where the turbulent eddy viscosity μ_T is calculated as in Eq. (1) for the CH model and $\sigma_{ij,T} = 1.0$.

Table 2. Dimensions of the grid.

Block	i	j	k	Σ
1	64	32	64	131 072
2	192	32	64	393 216
3	64	32	64	131 072
Total				655 360

4 Results

The layout of the return channel and the main dimensions in millimeters are presented in Fig. 1. A deswirl cascade has 14 blades. The inlet is at station 5, where experimental values are used as a boundary conditions. A detailed geometry description can be found in [6].

Only one deswirl channel is modelled. The grid is divided into three blocks: the first block is at the crossover, the second one is an O-type grid over a deswirl cascade, and the third is after the cascade. The grid dimensions can be seen in Table 2. The height of the first row of cells is 6×10^{-6}m. As nondimensional distances this is on the average $y^+ \approx 1$ but on the leading edge y^+ has a maximum value of 6 in a small area.

At the wall the velocity components are set to zero. In the present case the wall is also assumed to be adiabatic and the kinetic energy of turbulence is set to zero. For the CH, CHR and SSG model the dissipation ($\tilde{\epsilon}$) gets a zero gradient at the wall. For the GS model

$$\epsilon_{wall} = 2\nu \left(\frac{\partial \sqrt{k}}{\partial y_n} \right)^2 \tag{29}$$

For the calculation of the surface fluxes themselves a second-order extrapolation is applied for the evaluation of the wall pressure, and one-sided formulae are used for the derivatives in the diffusion terms.

The computational domain begins at station 5 (see Fig. 1). Experimental values are set for velocities and the average inlet Mach number is 0.15. For turbulence quantities the 10% turbulence intensity is assumed and the dissipation is assigned so that a nondimensional turbulent viscosity (μ_T/μ) is 100 in order to get a fully turbulent inflow. For the Reynolds stresses, isotropic turbulence is considered and the shear stresses are assumed to be zero. The static pressure is extrapolated from the computational domain. At the outflow boundary the static pressure is fixed and a zero gradient is assumed for the rest of the variables. To avoid errors from the outlet, station 8 is eight grid cells (27.9 mm) before the outflow boundary.

Table 3. Total pressure drop.

	Exp.	CH	CHR	GS	SSG
Δp_0 (N/m^2)	1977	730	3000	760	880

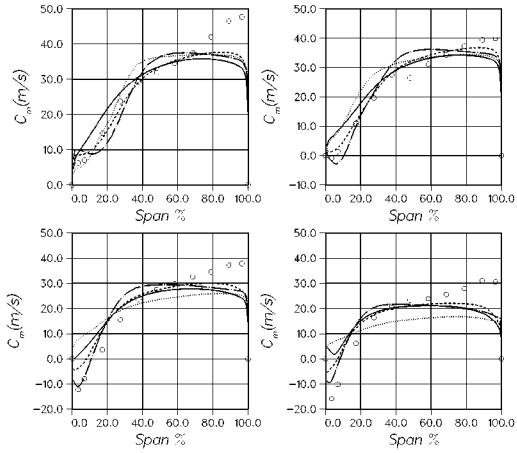

Figure 2. Meridional velocity at the blade pitches of 20, 40, 60 and 80 percents from the hub to the shroud (station 6). CH:—, CHR:· · ·, GS:- - -, SSG: — - — -.

4.1 Total Pressure Drop

The total pressure drop given in Table 3 is quite small in comparison with the pressure level, and it seems that numerical errors may have some effect on the calculation of Δp_0. The experimental value is higher than the simulated one except for the CHR model. The CHR model overpredicts the total pressure drop in comparison with the experimental data and other calculations. One reason for the higher total pressure drop of the experimental data can be explained if the walls are not hydrodynamically smooth. The difference between the SSG and the GS models may be caused by the current low-Reynolds number version of the SSG model, which generally overpredicts the skin friction.

4.2 Velocity Profiles at Different Stations

Measurement station 6 is after the crossover at the leading edge of the deswirl cascade (see Fig. 1). Profiles for the meridional and tangential velocities are shown in Figs. 2 and 3. The SSG and GS models seem to predict

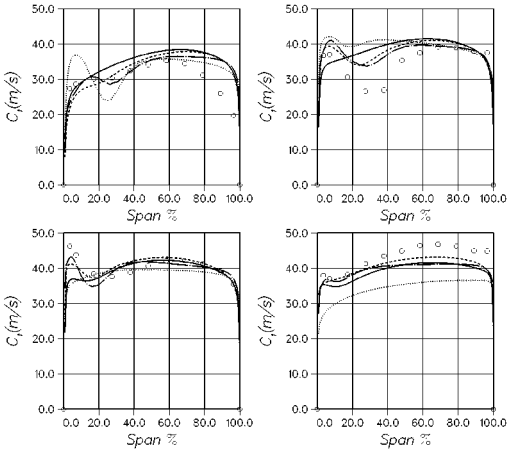

Figure 3. Tangential velocity at the blade pitches of 20, 40, 60 and 80 percents from the hub to the shroud (station 6).CH:—, CHR:· · ·, GS:- - -, SSG: — - — -.

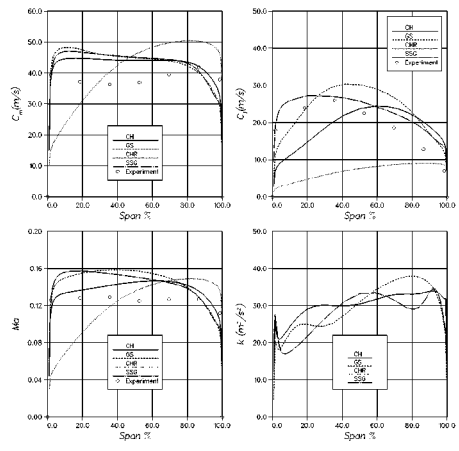

Figure 4. Pitch-averaged meridional and tangential velocities, Mach-number and kinetic energy of turbulence from the hub to the shroud at station 8.

the flow better than the simpler CH and CHR models. For example, the tangential velocity at blade pitch 60% (Fig. 3) contains a peek close to the hub that is predicted by the SSG model. Also the GS model predicts the peek, but it is smaller. The CH and CHR models do not seem to capture this phenomenon. All the turbulence models have difficulties at the shroud at all the pitch values. They underpredict the meridional velocities and overpredict the tangential velocities. The size of the separation bubble is seen from the meridional velocities in Fig. 2. The SSG model predicts the strength and the size of the bubble well. The CH and CHR models do not have a separation bubble at all at this station.

Station 8 is located 47.8 mm after the bend. Pitch-averaged values are shown in Fig. 4. Meridional velocities are predicted as well for the CH, GS and SSG models. The CHR model gives an excessively paraboloidal velocity profile. It can be concluded that the rotational correction in the suggested form does not work properly in the present case. Only the SSG model predicts the right shape of the tangential velocity at station 8.

4.3 Particle Traces

Particle traces are drawn at the center of the channel in Fig. 5. The CH model does not predict the separation after the crossover, which is a typical and expected feature. The CHR model predicts the separation, but it seems to take place too early and it also reattaches too early. The

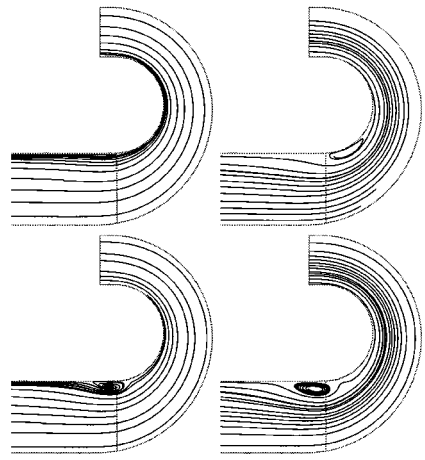

Figure 5. Particle traces in the center of channel at the crossover (CH, CHR, GS and SSG).

GS and SSG models have separation bubbles just after the bend.

Surface streamlines are shown in the case of the GS model in Fig. 6. Complex three dimensional separations and vortices are seen in the flow field. For example, at the leading edge of the vane, separation occurs on the pressure side. Separation takes place also at the trailing edge.

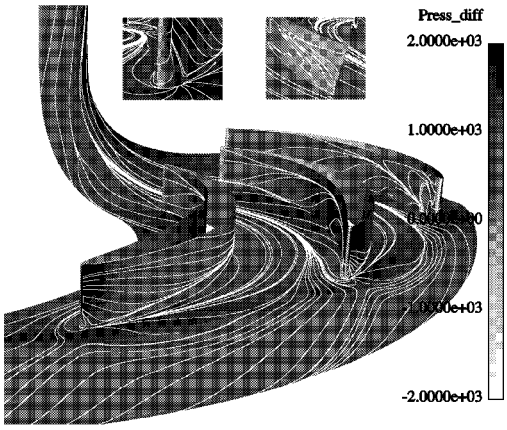

Figure 6. Surface streamlines at the deswirl cascade and the bends with the GS model. The inset figures are from the leading and trailing edge regions.

5 Conclusions

A simulation of a deswirl cascade has been performed using several turbulence models. A comparison is made between the predictions of different models and experimental results.

A comparison with the experimental data shows that the anisotropic models perform better than the two-equation models. This is especially true at station 6, after the crossover on the hub. However, at the shroud the situation is less encouraging also for the anisotropic models. All the turbulence models predict a similar behaviour which deviates considerably from the experimental data. The CHR model does not give good results for this case. It has been optimized by the authors for the rotating channel and applied successfully for a pump [9], but in the present form it is not a general solution to take account of the streamline curvature.

In complex geometries with a streamline curvature, the simulation of 3D effects and flow separation often fails with the $k-\epsilon$ model. This is due to the isotropic Boussinesq approximation as well as the history effect of different Reynolds stresses. The best results in the present case are achieved by the SSG model, although there are certain features that are systematically ill-predicted by all turbulence models. Also the GS model gives satisfactory results for some details not captured by the basic CH model.

REFERENCES

[1] R. Abid, C. Rumsey, and T.B. Gatski, 'Prediction of nonequilibrium turbulent flows with explicit algebraic stress models', *AIAA*, **33**(11), 2026–2031, (1995).

[2] K.-Y. Chien, 'Predictions of channel and boundary-layer flows with a low-Reynolds-number turbulence model', *AIAA Journal*, **20**(1), 33–38, (Jan 1982).

[3] L. Davidson and A. Rizzi, 'Navier–Stokes stall predictions using an albebraic Reynolds-stress model', *Journal of Spacecraft and Rockets*, **29**(6), 794–800, (1992).

[4] T.B. Gatski and C.G. Speziale, 'On explicit algebraic stress models for complex turbulent flows', *Journal of Fluid Mechanics*, **254**, 59–78, (1993).

[5] J. H. G. Howard, S. V. Patankar, and R. M. Bordynuik, 'Flow prediction in rotating ducts using coriolis-modified turbulence models', *Journal of Fluids Engineering*, **102**, 456–461, (Dec. 1980).

[6] D. Japikse and K. Oliphant, 'Return channel, swirl generator rotor and desweirl cascade'. ERCOFTAC Turbomachinery Workshop Test Case F3, 1998.

[7] A. Khodak and C. Hirsch, 'Second order non-linear k-ϵ models with explicit effect of curvature and rotation', in *Proceedings of the Third ECCOMAS Congress*, pp. 690–696, Paris, (Sept. 1996). John Wiley & Sons, Ltd.

[8] B. E. Launder, G. J. Reece, and W. Rodi, 'Progress in the development of a Reynolds-stress turbulence closure', *Journal of Fluid Mechanics*, **68**, 537–566, (1975).

[9] J. Ojala, P. Rautaheimo, and T. Siikonen, 'Numerical simulation of a centrifugal pump using a $k-\epsilon$ model including the effects of rotation', in *Proceedings of the Fourth ECCOMAS Congress*, Athens, (Sept. 1998). John Wiley & Sons, Ltd.

[10] P. Rautaheimo and T. Siikonen, 'Implementation of the Reynolds-stress turbulence model', in *Proceedings of the Third ECCOMAS Congress*, Paris, (Sept. 1996). John Wiley & Sons, Ltd.

[11] P.L. Roe, 'Approximate Riemann solvers, parameter vectors, and difference schemes', *Journal of Computational Physics*, **43**, 357–372, (1981).

[12] N. Shima, 'A Reynolds-stress model for near-wall and low-Reynolds-number regions', *Journal of Fluids Engineering*, **110**, 38–44, (1988).

[13] T. Siikonen, 'An application of Roe's flux-difference splitting for the $k-\epsilon$ turbulence model', *International Journal for Numerical Methods in Fluids*, **21**, 1017–1039, (1995).

[14] T. Siikonen and H. Pan, 'Application of Roe's method for the simulation of viscous flow in turbomachinery', in *Proceedings of the First European Computational Fluid Dynamics Conference*, pp. 635–641, Brussels, (Sept. 1992). Elsevier Science Publishers B.V.

[15] C.G. Speziale, S. Sarkar, and T.B. Gatski, 'Modelling the pressure-strain correlation of turbulence: and invariant dynamical systems approach', *Journal of Fluid Mechanics*, **227**, 245–272, (1991).